



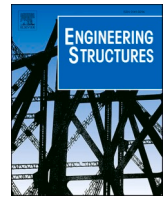
Numerical assessment of bond-slip relationships for naturally corroded plain reinforcement bars in concrete beams

Downloaded from: <https://research.chalmers.se>, 2024-07-27 04:10 UTC

Citation for the original published paper (version of record):

Yu, X., Robuschi, S., Fernandez, I. et al (2021). Numerical assessment of bond-slip relationships for naturally corroded plain reinforcement bars in concrete beams. *Engineering Structures*, 239. <http://dx.doi.org/10.1016/j.engstruct.2021.112309>

N.B. When citing this work, cite the original published paper.



Numerical assessment of bond-slip relationships for naturally corroded plain reinforcement bars in concrete beams

Xiaotong Yu^{a,b}, Samanta Robuschi^{c,*}, Ignasi Fernandez^c, Karin Lundgren^c

^a Key Laboratory of Coastal Disaster and Defence (KLCDD), Hohai University, Nanjing 210098, China

^b College of Harbor, Coastal, and Offshore Engineering, Hohai University, Nanjing 210098, China

^c Division of Structural Engineering, Department of Architecture and Civil Engineering, Chalmers University of Technology, 41296 Göteborg, Sweden

ARTICLE INFO

Keywords:

Corrosion
Plain reinforcing bars
Bond
FE analyses
Reinforced concrete

ABSTRACT

Reinforced Concrete (RC) heritage structures are often affected by corrosion. Consequently, knowledge about the effect of corrosion on the bond between reinforcing bars and surrounding concrete is critical when assessing the structural performance of these structures. In earlier work, structural tests were carried out on segments of edge beams taken from a decommissioned RC bridge. The specimens had naturally corroded plain reinforcement bars and three-point bending tests were conducted, to investigate their anchorage capacity. In this study, non-linear finite element analyses (NLFEA) were carried out to gain further insight into the bond behaviour of the tested specimens, including the effect of corrosion on the bond-slip relationship. Two different, one-dimensional (1D), bond-slip relationships were calibrated for each tested bar, to account for loss of bond upon yielding. The calibration process was based on a comparison between significant numerical and experimental results, including load–deflection curve, crack pattern and asymmetrical distribution of the yield penetration along the length of the bar. Good agreement between the FE analyses and experimental tests was observed. Finally, the calibrated bond-slip relationships for nine beams with different corrosion levels, casting positions, and visual damage are presented and discussed. The loss of bond at yielding and yield penetration asymmetry are both shown to be crucial factors for adequately describing structural behaviour.

1. Introduction

Corrosion of reinforcing bars is a major cause of deterioration in reinforced concrete (RC) structures. Corrosion reduces the cross-sectional area of the bar, leads to concrete cracking and cover spalling, and affects the bond between bar and concrete [1]. As corrosion propagates, the serviceability and safety of RC structures are seriously affected. Since many existing structures are deteriorated due to reinforcement corrosion [2], reliable methods of assessing the performance of these structures are needed urgently.

Numerous studies have been conducted on the effect of corrosion on the structural performance of RC beams. Based on experimental results [3–6], by decreasing both ductility and reinforcement area [7], corrosion may lead to alterations in the failure mode, (from flexure to shear, shear-compression or anchorage, for example) and reduce the load-carrying capacity of the structure. However, it should be noted that the majority of studies focused on ribbed reinforcing bars, as these had become the norm in construction from around the mid-1950s in America

and Canada and around the mid-1960s in Europe [8]. Even so, plain bars are still widely present in historical RC structures which, in many cases, now require assessment and rehabilitation [8]. Only a few studies of beams which include corroded plain bars are available in the current state-of-the-art [9–11] and the behaviour they describe differs significantly, as compared to corroded RC members with ribbed bars.

One important underlying aspect is the difference in bond mechanisms between ribbed and plain bars. This means there is an anticipated difference in the impact of corrosion on their bond mechanisms. The main difference between plain and deformed bars is the lack of ribs. The mechanical interlock between ribs and concrete is the major component in the bond of deformed bars, while the bond in plain bars fundamentally depends on the adhesion and friction of the bar-concrete interface [12]. The different bond mechanisms indicate that the results obtained from deformed bars cannot be directly extended to plain bars [8,13].

A limited number of bond-slip relationship for plain bars can be found in codes and literature. In Fig. 1, three examples are presented. The bond-slip relationship for plain bars in Model Code 2010 [34] is

* Corresponding author.

E-mail address: samanta.robuschi@chalmers.se (S. Robuschi).

<https://doi.org/10.1016/j.engstruct.2021.112309>

Received 2 July 2020; Received in revised form 24 March 2021; Accepted 29 March 2021

Available online 9 April 2021

0141-0296/© 2021 The Authors. Published by Elsevier Ltd. This is an open access article under the CC BY license (<http://creativecommons.org/licenses/by/4.0/>).

calculated as a function of the concrete compressive strength expressed in MPa. Good and poor bond conditions (depending on the placement and confinement of the bar) are distinguished, and a reduction factor of 0.5 is suggested for poor conditions. The bond-slip relationship is described by an ascending non-linear curve up to the maximum bond stress, followed by a constant branch. The slip corresponding to the maximum bond stress is constant and equal to 0.1 mm. Other bond models can be found in the literature for uncorroded plain bars, most commonly based on the results of pull-out tests. Verderame et al. [38] proposed a bond-slip model with as well an initial non-linear branch, but with a larger slip value at peak; 0.23 mm. The model introduces a linear descending branch for the after-peak behavior, followed by a plateau. The compressive strength of the concrete remains the main parameter for the definition of the maximum bond strength. A third bond-slip constitutive model worth mentioning is by Feldman and Bartlett [10]. Their empirical model differs from the others in the use of a non-linear descending branch and in including parameters in addition to the compressive strength for the calculation of the bond strength: the roughness of the bar (R_y) and the embedded length (l_d).

However, there is a dearth of available research on the bond behaviour of corroded plain bars [13–16]. Such studies indicate relevant parameters (such as corrosion level, presence of confinement, cover thickness, bond at yielding and the initial condition of the bars) that influence the bond behaviour. Also, the casting position (top or bottom-cast) was deemed a highly significant factor due to the varying density of the concrete surrounding the bar and, thus, the possibility of corrosion products accumulating in the cement pores [11,13]. Additionally, there are concerns about using results obtained from artificially corroded specimens to predict the behaviour of naturally corroded bars [17–19,39].

Modelling, specifically nonlinear finite-element analyses (NLFEA), is a widely used tool [20,21] to improve our understanding of how the bond between concrete and naturally corroded plain bars is affected by corrosion products. Detailed bond and corrosion models are often

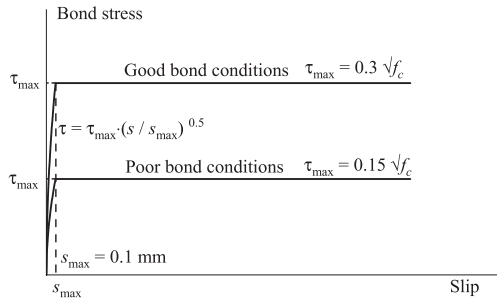
implemented at interface elements between reinforcement and concrete, in three-dimensional (3D) NLFEA [22,23]. However, considering the computational cost and amount of data needed, such an approach may be impractical for assessing entire structural systems. A pre-defined, one-dimensional (1D) bond-slip relationship in 3D NLFEA has already been proved as a valid alternative; it provides a reliable and time-efficient description of structural behaviour [21]. This method was chosen for this study, to examine the structural behaviour of beams with naturally corroded plain bars.

In reality, the beams were cut from the edge beams of a decommissioned bridge in Sweden, that had been previously tested by the authors [11]. For most of the beams, yielding of the reinforcement bars limited the load-carrying capacity. Yielding was followed by anchorage failure and, thus, the deformation capacity of the beams was limited. The loss of bond after yielding led to a change in the load-carrying mechanism, from beam to arch action.

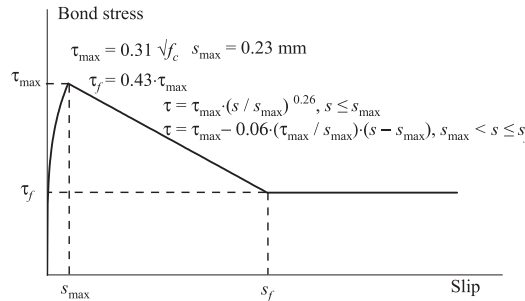
This study aims to improve understanding of the structural behaviour of the tested beams; more specifically, how the bond-slip relationship of plain reinforcement bars is affected by yielding and corrosion damage and how this, in turn, affects beam behaviour. Consequently, 3D NLFEA was conducted on the tested beams, including individually calibrated bond-slip curves for each reinforcing bar. To account for the effect of yielding on bond behaviour, the tensile bars are divided into yielded and unyielded zones in the FE model, with distinct bond-slip relationships assigned. By comparing simulation results with experimental measurements, the NLFE models (and, thereby, the 1D bond-slip relationships) are calibrated and validated for each bar in the nine tested beams. Finally, the overall numerical results and calibrated bond-slip relationships are discussed.

2. Experimental program and materials

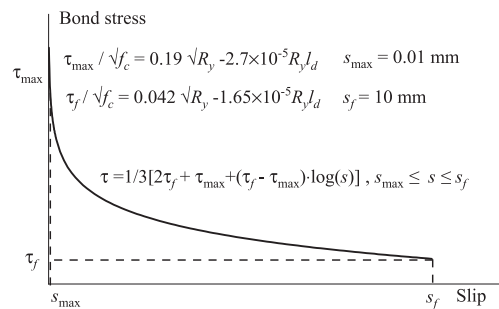
Gullspång Bridge (1935–2016) was a concrete bridge reinforced with plain steel bars and located in the town of Gullspång, Sweden. The



(a) CEB-FIP model code 2010 [34]



(b) Verderame et al. [38]



(c) Feldman and Bartlett [10]; R_y is the roughness of the bar and l_d the embedded length

Fig. 1. Bond-slip relationships for plain bars embedded in concrete.

bridge was exposed to different conditions during its service life, including freeze–thaw cycles and the use of de-icing salts. Heavy corrosion damage was visible in parts of the structure. The edge beams of the bridge were extracted before demolition and divided into smaller members for research purposes. The experimental study comprised two different investigations into the effect of corrosion on the bond of plain reinforcement bars; one focusing on structural behaviour [11] and one focusing on local bond strength [16].

During the structural investigation, twenty 900 mm beams were cut from the edge beams and classified according to the extent of visible corrosion damage within the anchorage zones. Three categories were defined: (1) reference beams (R), meaning beams with no visible cracks, (2) cracked beams (C), meaning beams with visible surface cracks, and (3) severely damage beams (S), meaning beams with corrosion-induced cracks and concrete spalling. The results of structural tests conducted on these members are presented in Robuschi et al. [11]. Nine out of twenty tested beams were selected and studied in this work.

2.1. Three-point bending tests

A three-point bending test set-up was used to bring the specimens to failure, see Fig. 2. The test configuration was designed to evaluate the influence of corrosion on the anchorage capacity of the tensile bars [24]. A narrow support (NS, 50 mm × 100 mm), was placed on one end of the beams, to minimise the confinement effect on the tensile reinforcements due to support pressure. A full support (FS, 50 mm × 250 mm), was used at the other end of the beam, to prevent the beam from tipping during loading. To assess the influence of the casting position of the bars (in other words, top or bottom-cast bars), the beams were positioned in two different configurations in the rig; as positioned on the bridge or upside down. For the present study, two beams were chosen as positioned on the bridge and seven upside-down. The reasons for testing more upside down beams were twofold; (1) because top-cast bars are known to have a weaker bond between concrete and steel and were therefore deemed more interesting and (2) because severe corrosion damage occurred, with bars falling off in the bottom inner position. Thus, there were not so many relevant results available for beams tested as positioned on the bridge.

2.1.1. Yield penetration and corrosion level of tensile reinforcement bars

After testing, the tensile reinforcement bars were carefully taken out of the beams. Corrosion products and concrete attached to the bar surface were removed by sandblasting, according to [25]. The bars were then 3D-scanned. This allowed the yielded parts of the bars to be located and their average corrosion level to be estimated, by calculating the average loss of cross-sectional area in the unyielded segments according to [11]. Geometrical information (such as the uncorroded area and perimeter) was also obtained for each bar by 3D scanning.

2.1.2. Results of the bending tests

The tests were characterized by the opening of one or two major

bending cracks, that was closely followed by yielding of the tensile reinforcements. In most of the tested beams, their load-carrying capacity was limited by yielding of the bars. After yielding, slipping of the two tensile reinforcement bars occurred at different deflections, as shown in Fig. 3. However, the failure was defined as a bending failure, since slipping of the bars occurred at a point where the bending cracks had already reached an opening width of several centimetres. Of the nine modelled beams, only two failed in anchorage before the tensile reinforcement yielded.

This study numerically models the behavior of the beams in 3-point bending and makes use of the experimental measurements both as input for characterizing the bond of the naturally corroded, plain reinforcing bars and for the calibration of the FE models.

Three parameters were of particular importance: mid-span deflection at end-slip, loss of load capacity at end-slip and yield penetration along the length of the bar. The mid-span deflection and loss of load capacity at end-slip were critical for the calibration of bond-slip relationship (as discussed in Section 4). The yield penetration was preassigned to allowed for the use of simple, 1D bond-slip relationships, as explained in the following. The corrosion level of the rebars was as well pre-assigned in the model, while the crack pattern and crack widths were used in the calibration procedure.

The need for pre-assigning the yield penetration in the model was due to the asymmetric yield penetration along the length of the bars observed in the tests. This caused the unyielded length at the side where anchorage failure took place being significantly shorter than at the other side of the beam, see Fig. 4. This behaviour was observed for most of the tested beams, despite the loads being equidistant from the supports. Factors such as heterogeneity of the material properties of the concrete, non-uniform corrosion along the bar, unequal stirrups disposition and use of different support types (full and narrow support), are likely linked to the asymmetrical distribution of the yield penetration. To evaluate this asymmetry, an asymmetry factor (α) was defined as:

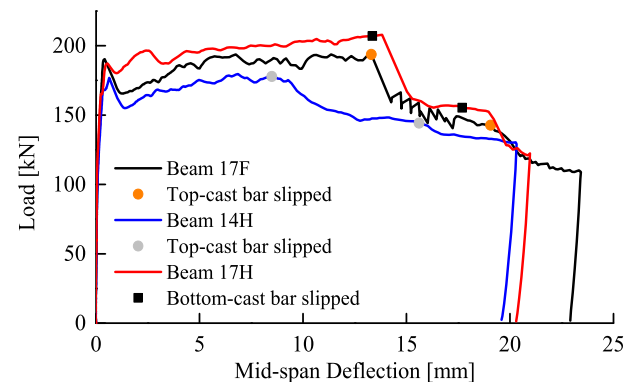


Fig. 3. Typical load versus mid-span deflection curves in beam tests, examples of 17F, 14H, and 17H.

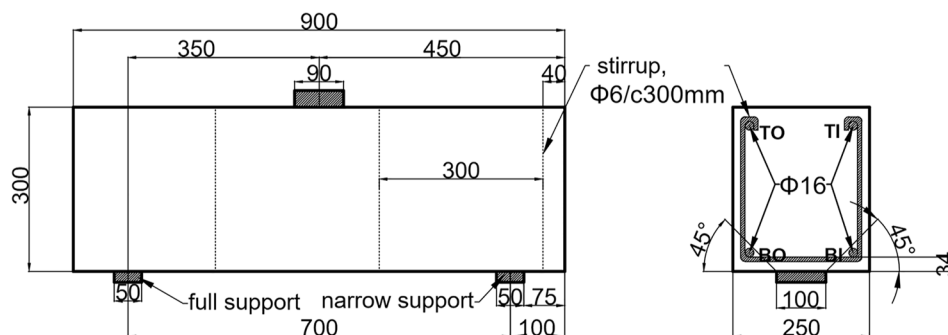


Fig. 2. Test set-up and view of narrow support in the beam tests [11]. The beam shown was tested as positioned on the bridge. Measurements in mm.

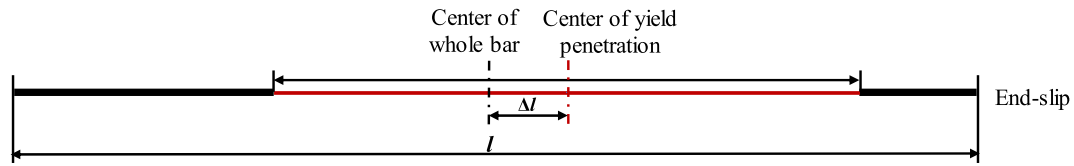


Fig. 4. Parameters used to define the asymmetry factor (a) in this study.

$$a = \Delta l / 0.5l \quad (1)$$

where Δl is the difference between the centre of the bar and the centre of the yielded region, and l is the total bar length, Fig. 4.

2.2. Properties of concrete used in the analyses

Material tests were conducted on concrete cylinders drilled from the edge beams. A total of eight uniaxial compression tests were conducted to determine the compressive strength (f_c) [11]. The modulus of elasticity (E_{cm}) was obtained from three uniaxial compression tests. Additionally, splitting tensile tests were conducted on four additional cylindrical samples, according to EN 12390-6:2009 [26]. The fracture energy (G_f) was calculated from the compressive strength according to CEB-FIP Mode Code 90 [27], assuming the maximum aggregate size to be 16 mm. The concrete material parameters used in the analyses are provided in Table 1.

2.3. Tensile properties of reinforcement bars

Tensile tests were carried out on bar segments cut from the unyielded zones of each tensile reinforcement. Detailed information on the tensile tests is provided in [11]. The average corroded cross-sectional area of the corresponding segment was used to calculate the tensile stress. The stress-strain curve obtained from the tensile test of each bar was used as input to the corresponding reinforcement element in the model. For five of the bars, no information was available; due to damages resulting from the extraction process, they could not be tested. However, all the bars in the beams had similar properties, and similar load-displacement curves [16]. Therefore, the yield stress in these bars was assumed equal to the average yield stress of uncorroded tested bars (see Fig. 5). This is based on the assumption that the yield stress does not change with corrosion at low corrosion levels; this is consistent with observations in several studies [36,37]. The main properties of each curve, such as yield stress (f_y), yield strain (ϵ_y), ultimate stress (f_u) and ultimate strain (ϵ_u) are listed in Table 2. The bars are labelled according to their position in the cross-section of the beam; TI (top-cast, inner side of the bridge), TO (top-cast, outer side of the bridge), BO (bottom-cast, outer side of the bridge) and BI (bottom-cast, inner side of the bridge) (see Fig. 2).

3. Numerical modelling

This section introduces the 3D NLFE analyses of the presented beams. The analyses were used to simulate their structural performance, with 1D bond-slip relationships used to represent the bond between the naturally corroded plain bars and the concrete.

Table 1
Properties of concrete used in the analyses.

Parameter	Value
Mean compressive strength f_c	45.6 MPa
Mean modulus of elasticity E_{cm}	27.4 GPa
Poisson's ratio ν	0.15
Mean tensile strength f_t	2.93 MPa
Fracture energy G_f	90 N/m
Crack band width h_b	0.02 m

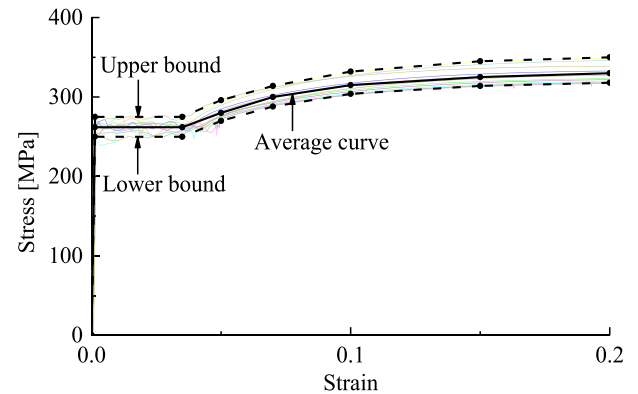


Fig. 5. Upper and lower bound of the stress-strain curves and average stress-strain curve used in the model.

Table 2

Tensile properties of reinforcement bars used in the analyses.

Beam	Bar	Yield stress f_y (MPa)	Yield strain ϵ_y	Ultimate stress f_u (MPa)	Ultimate strain ϵ_u
17F	TI	260	0.0013	332	0.2
	TO	260	0.0013	323	0.2
17H	BO	265	0.00133	350	0.2
	BI	255	0.00128	327	0.2
9D	BO	262	0.0013	330	0.2
	*				
10I	BI	260	0.0013	317	0.2
	TI	265	0.00133	323	0.2
10I	TO	262	0.0013	330	0.2
	*				
13D	TO	260	0.0013	320	0.2
	TI	265	0.00133	325	0.15
16B	TI*	262	0.0013	330	0.2
	TO	270	0.00135	338	0.2
16H	TI	255	0.00128	320	0.2
	TO	262	0.0013	330	0.2
16K	TI*	262	0.0013	330	0.2
	TO	265	0.00133	328	0.2
14H	TI	260	0.0013	318	0.2
	TO	265	0.00133	345	0.2

* Average tensile properties, as described in Fig. 5.

3.1. FE model description

The finite element software DIANA 10.2 [28] was used for the analyses. The geometry of each model was based on the specific measurements of the corresponding specimen. An overview of a 3D model is shown in Fig. 6. Spalling of concrete cover was included in the model by removing the concrete surrounding the bar at the spalled locations, as shown in Fig. 6b. Corrosion of the reinforcement was implemented as an average cross-sectional reduction of reinforcement area in the unyielded segments. Corrosion was not considered in the cross-section of the yielded segment of the reinforcement bar; due to the deformation induced by yielding, it was not possible to calculate the average corrosion level of the segments with 3D scanning data. The influence of corrosion damages on the yielding behaviour was however observed to

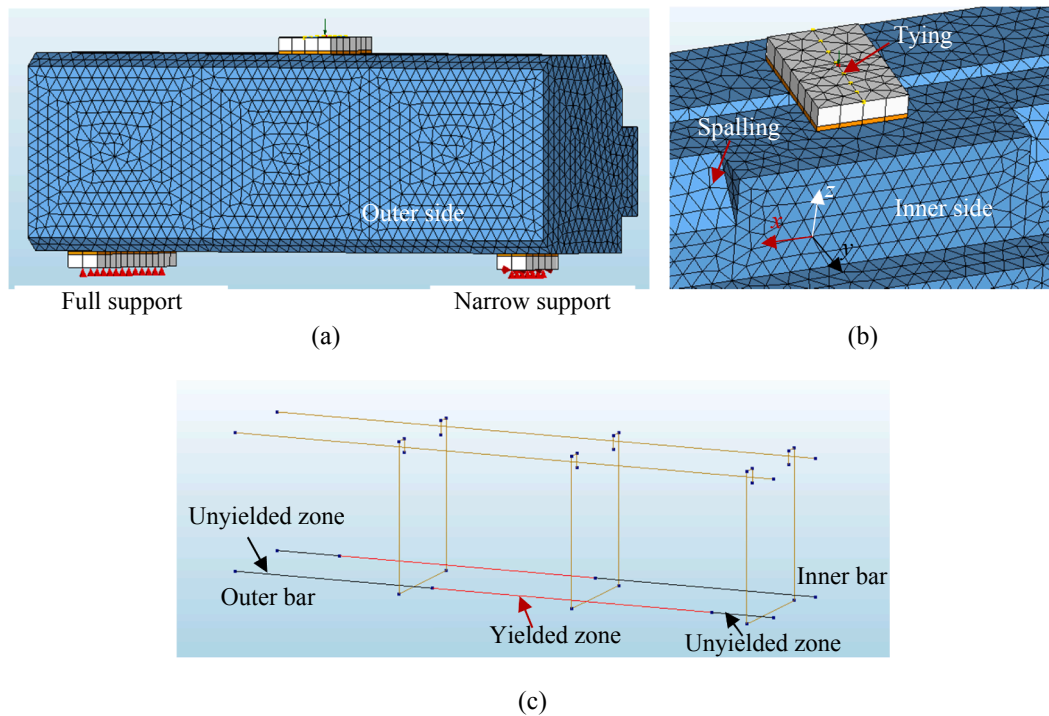


Fig. 6. Overview of an FE model for a tested beam: (a) 3D FE model with boundaries; (b) details at the loading plate, with the inclined surface corresponding to where the cover was spalled off; (c) layout of reinforcement bars.

be negligible; likely due to the relatively small corrosion levels, 1–2%.

3D tetrahedral elements (TE12L) were used for the concrete. The longitudinal tensile reinforcement bars were modelled using embedded reinforcement with 1D bond-slip relationships. The bond-slip relationships were described by multi-linear curves. By contrast, the compressive reinforcement bars and stirrups were modelled as fully bonded and using embedded reinforcement elements, see Fig. 6c. The loading plate and supports consisted of a steel plate and a wood one (as in the tests) and were modelled using triangular-prism elements (TP18L). The geometrical dimensions of support and loading plates were also the same as in the test set-up. The full support (FS) was restrained in the vertical direction, while the narrow support (NS) was restrained in both vertical and longitudinal directions. The load was applied via displacement control on a master node at the top of the steel loading plate. A line of nodes was tied to the master node; this allowed rotation of the plate around the y-axis but imposed the same displacement in z-direction.

An incremental static analysis was conducted, using specified displacement increments. These increments were set to a vertical displacement (z-axis) of 0.01 mm until a 1 mm mid-span deflection was reached. The increments were then increased to 0.2 mm to save computation time. The analyses were conducted using a Quasi-Newton (BFGS) scheme, based on force and energy convergence criteria, with respective tolerances of 0.01 and 0.0001.

3.2. Material models for concrete and steel reinforcement

For concrete, a total strain-based rotating crack model (using nonlinear fracture mechanics) was chosen to describe cracking. The tensile behaviour was modelled using a stress-strain curve proposed by Hordijk [29]. The crack band width (h_f) was assumed as equal to the average element size of 0.02 m. This assumed size of the localization zone was later verified in the analysis results. The compressive behaviour of concrete was described by an ideal elasto-plastic relationship. The reduction of compressive strength due to lateral cracking was taken into account using a model developed by Vecchio and Collins [30]. The stress confinement was also taken into account, as suggested by Selby

and Vecchio [31]. The concrete properties used in the analyses are listed in Table 1.

The steel reinforcement was modelled using a Von Mises plasticity model, including strain hardening. A simplified multilinear curve obtained from tensile testing of each individual bar was used as input. The tensile properties of the reinforcement bars are provided in Table 2.

3.3. 1D bond-slip relations

As shown in different studies, bond is strongly affected by bar yielding [32,33]. This phenomenon is even more relevant with plain bars than ribbed ones, as a major part of the bond capacity comes from friction. Since the experimental tests were significantly affected by yielding of the tensile reinforcement bars, the loss of bond at yielding needed to be included in the modelling. Thus, the bars were divided into different zones according to test measurements, as shown in Fig. 6c. Also, two different bond-slip relationships were defined for each bar in the analyses; one for the yielded zone and another for the unyielded zones.

The so-called yielded zone was defined over the length of the bar affected by yield penetration, as measured after the tests. However, it should be noted that assigning a single bond-slip relationship to all sections of the bars that yielded during testing is a simplification. Thus, the bond-slip relationship given to the yielded zone does not correspond to the bond-slip curve of a yielded bar. Rather, the bond-slip curve of the yielded zone is designed to describe the bond at the beginning of the test (when the bar was unaffected by yielding) and the subsequent loss of bond associated with yielding. Note that the tensile properties was the same in the yielded and unyielded zones. Thus, the bond-slip relationship was the only parameter changed. It can also be noted that the same bond-slip relationship can be expected in both regions before the reinforcement yields; the chosen division of different bond-slip relationships in yielded and unyielded zones was made to simplify the analyses.

Fig. 7 describes the bond-slip relationships used for the yielded and unyielded zones. Such relationships were defined by nine different parameters; five for the unyielded bond-slip and four for the yielded one.

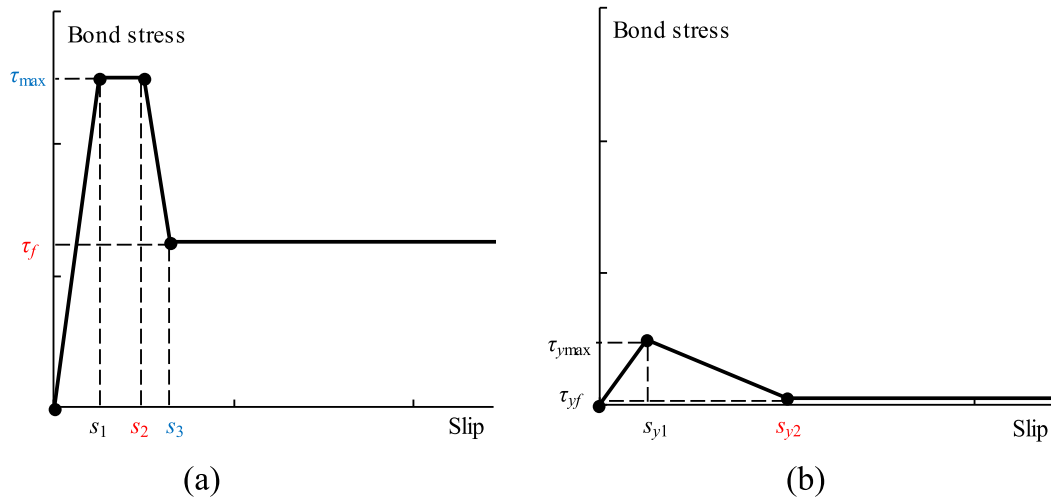


Fig. 7. Bond-slip relationships for (a) unyielded zones and (b) yielded zone. The parameters are divided into three sets: 1 (black), with the same values for all bars; 2 (blue) calculated manually and 3 (red) calibrated individually. (For interpretation of the references to colour in this figure legend, the reader is referred to the web version of this article.)

The nine parameters were divided into three sets (highlighted in different colours in Fig. 7), due to different roles in the calibration procedure (details in Section 4). The bond-slip relationship for the unyielded zones resembles the one proposed in CEB-FIP Mode Code 2010 [34], which is characterised by four branches; ascending, plateau, descending and residual. The following parameters define the transition between branches: τ_{\max} and τ_f are, respectively, maximum bond stress and residual bond stress for unyielded zones; s_1 and s_2 are the slips at the start and end of the maximum bond stress plateau. Finally, s_3 corresponds to the slip when residual bond stress is reached. However, the bond-slip relationship for the yielded zone consists of only three branches; ascending, descending and residual. Thus, no plateau is included for the yielded zone. The main parameters defining the transition between branches are $\tau_{y\max}$ and τ_{yf} (representing maximum and residual bond stresses respectively) and s_{y1} and s_{y2} (corresponding to the slip at maximum bond stress and slip at the beginning of the residual bond stress branch respectively). In addition, at the steel concrete interface the normal stiffness modulus was set to 2×10^{14} N/m³, while the shear stiffness modulus was calculated as τ_{\max}/s_1 , $\tau_{y\max}/s_{y1}$.

4. Calibration procedure of bond-slip parameters

As explained in the previous section, nine unknown parameters characterise the bond-slip relationships in a single bar. This section presents the calibration process for these parameters. Assumptions and interpretations about the influence of each parameter on the structural behaviour are described, plus the calibration methodology used. As an example of the parameter calibration process, a thorough description is given of the entire process for a single tensile reinforcement bar; namely TO in beam 17F. Note that, once the manually calculated, fixed parameters are defined for both bars, the calibration for a single bar in the beam becomes essentially independent of the other bar. To conclude, the model and, consequently, the calibration of the bond relationships, is validated against the experimental results by thoroughly comparing various aspects; load-deflection, crack pattern, crack width, yield penetration and yield penetration asymmetry.

As mentioned earlier, the nine parameters representing the bond-slip relationship of each yielded tensile bar were grouped into three sets and highlighted in different colours, Fig. 7. The first set contains parameters chosen to have the same values for all bars. This includes $\tau_{y\max}$, τ_{yf} , s_{y1} and s_1 . The second set contains two parameters manually calculated from test results, τ_{\max} and s_3 . The third set consists of three parameters, τ_f , s_{y2} and s_2 ; these were calibrated by comparing the results of the FE

analyses with the experimental results for each beam individually. The bars that slipped before yielding only required determination of five parameters, since only the bond-slip relationship for the unyielded zone was used. A parametric study was undertaken, to understand the influence of each parameter on the structural behaviour of the modelled beam. An overview of the results appears in Table 3.

4.1. Constant parameters

The parameters $\tau_{y\max}$, τ_{yf} , s_{y1} and s_1 were chosen to have constant values for all bars, based on similarities in their influence on the anchorage behaviour of the various beams. This is described and discussed in more detail for each parameter below.

4.1.1. Maximum bond stress for yielded zone, $\tau_{y\max}$

The maximum bond stress for the yielded zone, $\tau_{y\max}$, describes the maximum bond reached before yielding took place in the predefined yielded zone. In reality, this value likely varies along the bar in the yielded zone. In areas close to the crack, where the bar first started yielding, the maximum bond stress was likely lower than in areas further from the crack. However, by way of simplification, this study chose a single value for the entire yielded zone. Upper and lower bounds were used to give trial values. Experimental results (in the form of a known force transfer along a known length of the bar when yielded), gave an estimate of 1 MPa [11]. This was deemed a lower bound, as it was affected by yielding. The upper limit was evaluated based on the bar reaching the yield force in the cracked section when the bar first started yielding. Thus, the average bond stress (acting along the distance between the first bending crack and the end of the beam) had to carry the yield force. This corresponded to a value of between 2.5 and 3 MPa in the different tested beams.

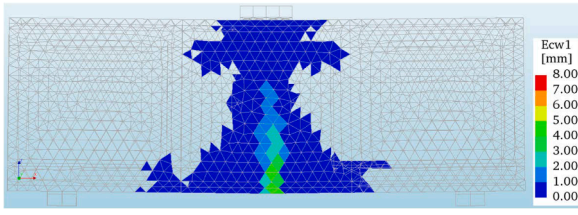
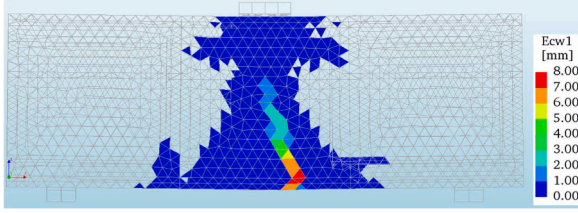
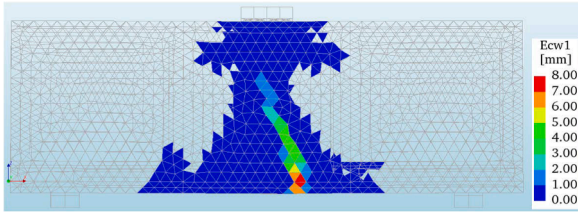
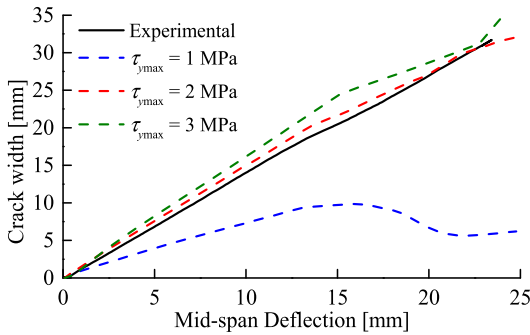
Accordingly, three $\tau_{y\max}$ values between these boundaries were investigated in the parametric study; 1, 2 and 3 MPa. It was observed that $\tau_{y\max}$ largely affected crack width and mid-span deflection (Δ_m) at end-slip. Fig. 8 shows the crack pattern and crack width in the various analyses. As may be observed in Fig. 8d, the results for $\tau_{y\max}$ equal to 2 or 3 MPa showed good agreement for crack width, while a value of 1 MPa underestimated it. Further, in Table 3, it may be seen that $\tau_{y\max}$ equal to 1 or 2 MPa gave reasonable values for the mid-span deflection at end-slip, while $\tau_{y\max}$ equal to 3 MPa did not. Accordingly, $\tau_{y\max}$ at 2 MPa was chosen, as this value gave the best agreement for both crack width and mid-span deflection at end-slip.

As most of the beams showed similar crack patterns (one major crack

Table 3

Experimental results from testing of beam 17F are compared to results obtained with the calibrated bond-slip curve. The results of a parametric study conducted on the bond-slip curve of the Top-Outside bar are as well shown. The parameters are varied one at a time, while the other parameters of the bond-slip curve are kept equal to the final calibrated value.

Experimental results										Mid-span deflection at end-slip (mm)	Residual load capacity (kN)	Yield penetration at failure (mm)	Asymmetry factor (a = Δl/0.5 l) (%)	
Beam 17F										19.1	110.9	463	24.2	
FE Analyses		Bond- slip parameters								Analysis results				
Analysis type		τ _y max (MPa)	τ _y f (MPa)	s _y 1 (mm)	s ₁ (mm)	τ _{max} (MPa)	s ₃ (mm)	τ _f (MPa)	s _y 2 (mm)	s ₂ (mm)	Mid-span deflection at end-slip (mm)	Residual load capacity (kN)	Yield penetration at failure (mm)	Asymmetry factor (a = Δl/0.5 l) (%)
Final analysis with calibrated-parameters		2	0.2	0.01	0.01	10.3	0.104	6	0.35	0.1	19.2	111.8	471	24.2
Varying parameter	Final calibrated value	Analyses with a variation of ±Δ with respect to the calibrated parameter												
τ _y max	2 MPa	3 1									22.7 17.9	110.3 111.9	477 468	22.9 24.5
τ _y f	0.2 MPa		0.4 0.6								22.5 No slip	113.7 No slip	480 462	23.1 21.1
s _y 1	0.01 mm			0.005 0.015 0.1							19.5 19.9 22.3	112.1 111.3 111.8	471 471 471	24.2 24.2 24.2
s ₁	0.01 mm				0.02 0.05 0.1						19.5 20.0 18.6	111.9 112.6 112.8	471 471 471	24.2 24.2 24.2
s ₃	0.104 mm						0.102 0.108				19.5 19.8	111.9 112.6	471 471	24.2 24.2
τ _f	6 MPa							5.5 6.5			19.5 18.7	107.1 115.4	471 471	24.2 24.2
s _y 2	0.35 mm								0.25 0.45		14.2 21.0	112.4 111.2	415 471	18.6 24.2
s ₂	0.1 mm									0.05 0.15	13.5 20.4	112.6 111.6	403 471	17.3 24.2

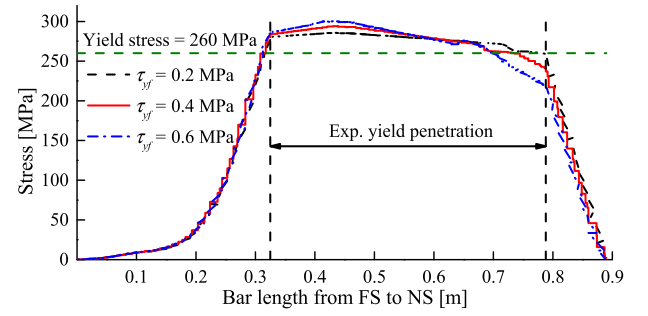
(a) $\tau_{y\max} = 1$ MPa. Contour plot of the crack width at $\Delta_m = 4.1$ mm.(b) $\tau_{y\max} = 2$ MPa. Contour plot of the crack width at $\Delta_m = 4.1$ mm.(c) $\tau_{y\max} = 3$ MPa. Contour plot of the crack width at $\Delta_m = 4.1$ mm.(d) Crack opening versus mid-span deflection for various $\tau_{y\max}$ values. The crack width obtained from experimental results appears in black.**Fig. 8.** Crack behaviour in the FE analyses, with varying $\tau_{y\max}$.

accompanied by a minor crack) and because the main focus was on reproducing the anchorage behaviour, this calibration was deemed sufficient. Thus, the same $\tau_{y\max}$ value of 2 MPa was used in all the models.

4.1.2. Residual bond stress for yielded zone, τ_{yf}

The residual bond strength of a yielded bar, τ_{yf} , is expected to be very small [11,32,33,35]. τ_{yf} values varying from 0.2 to 0.6 MPa were investigated. From the FE results, it was found that τ_{yf} equal to 0.2 or 0.4 MPa resulted in the anticipated failure mode (end-slip of the bar after yielding). The failure mode turned to concrete crushing when τ_{yf} was set to 0.6 MPa, without bar slippage. In this case, for comparison, the yield penetration and asymmetry values were measured just before concrete crushing.

The tensile stress distribution along the bar was also affected by the chosen τ_{yf} value. Fig. 9 describes the stress distributions of the bar at a mid-span deflection (Δ_m) of 19.2 mm (when the bar started slipping on the side with the narrow support) for different τ_{yf} values. From the results, it was concluded that τ_{yf} equal to 0.2 MPa produced better agreement in both yield penetration and stress distribution. High τ_{yf}

**Fig. 9.** Bar stress distributions at end-slip ($\Delta_m = 19.2$ mm) in the analyses of $\tau_{yf} = 0.2$.

values could transfer higher bond stresses, which shortened the yield penetration length and decreased the arch action in the mid-span. Thus, even though the bar was divided into yielded and unyielded zones from the beginning, the length and asymmetry of the yield penetration could only be described correctly when a small τ_{yf} value was applied. Given that a similar behaviour was observed in all the tested beams where yielding of the tensile reinforcements took place, τ_{yf} at 0.2 MPa was adopted for all the modelled beams.

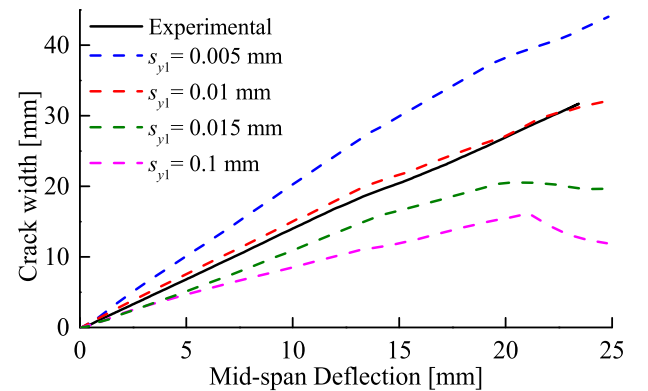
4.1.3. Slip corresponding to maximum bond stress for yielded zone, s_{y1}

The slip corresponding to maximum bond stress for the yielded zone was expected to be comparatively small, since the bars start yielding right after the opening of the bending crack, when the slip between bar and surrounding concrete is still limited. s_{y1} values ranging between 0.005 and 0.1 mm were investigated. The results in Fig. 10 and Table 3 show that s_{y1} mainly affected the crack width. Large s_{y1} values influenced the mid-span deflection at end-slip but to a lesser extent. The crack width was the main indicator of correct calibration of the parameter. As seen in Fig. 10, the crack width decreased as the s_{y1} value increased and the best agreement with experimental measurements was found for an s_{y1} value of 0.01 mm. Since the manner of yielding was similar for all the tested bars, $s_{y1} = 0.01$ mm was chosen as constant in this study.

4.1.4. Slip at the start of maximum bond stress for unyielded zones, s_1

According to [34], the slip corresponding to maximum bond stress for the unyielded zone, s_1 , is suggested to be around 0.1 mm. However, the code proposes an exponential curve for the initial branch of the bond-slip relationship. Since this work used a linear relationship instead, a lesser s_1 value was deemed a reasonable compensation. Therefore, the investigated s_1 values ranged between 0.01 and 0.1 mm.

As may be seen in Table 3, the numerical results for s_1 varied between

**Fig. 10.** Measured crack width compared to crack width output of the beam models, for different s_{y1} values. All results are plotted against mid-span deflection.

0.01 and 0.1 mm and showed almost no influence on the main structural parameters. In other words, mid-span deflection at end-slip, residual load capacity and yield penetration and asymmetry remained virtually constant, regardless of the value chosen. There was some influence on the crack width, see Fig. 11. With the increase in s_1 , the bond stiffness decreased and thus the crack width increased. s_1 was adopted at 0.01 mm; the same value as s_{y1} in this study. However, for the reasons outlined at the beginning of this section, it is noteworthy that the peak real slip of a plain reinforcement bar is probably slightly greater than this value [16].

4.2. Manually calculated parameters

The parameters τ_{\max} and s_3 were chosen to be manually calculated from test results, by assuming uniformly distributed bond stress in the unyielded zone on the end-slip side. This is described more in detail below. By calculating these from experimental results, it is possible to include the varying damage levels (corrosion and cracking) of the beams.

4.2.1. Maximum bond stress for unyielded zones, τ_{\max}

The assumption of uniformly distributed bond stress was used in the previous study to calculate the average bond strength in the unyielded zone at the end-slip side [11]. Although such assumptions are commonly used when calculating bond stress in short pull-out tests, the actual bond stress distribution before anchorage failure is unknown and may significantly deviate from uniformity. Fig. 12 depicts three examples of simplified bond distributions along the unyielded zone. All three have the same area under the curve, but they yield to different maximum bond stresses. For the sake of safety and simplification, this study adopted τ_{\max} as the average bond strength, according to the short pull-out hypothesis. This corresponded to the lower bound of possible maximum bond stresses.

4.2.2. Slip corresponding to residual bond stress for unyielded zones, s_3

The slip at the start of residual bond stress for unyielded zones (s_3 and s_2) defines the descending slope of bond-slip curves for unyielded zones. It may be noted that, in the case of a large difference between s_3 and s_2 , the bond distribution along the unyielded zone is closer to the piecewise linear bond stress shown in Fig. 12. In keeping with the assumption of uniformly distributed bond stress in the unyielded zone at the end-slip side, a small difference between s_3 and s_2 was chosen (a very stiff descending branch). Accordingly, the initial choice was to have the same stiffness for the descending slope as for the ascending slope, but with the opposite sign. This choice correlated with an s_3 value of 0.104 mm. As shown in Table 3, the influence on the results was small when s_3 varied between 0.102 mm and 0.108 mm. (Note that although the variation in s_3 may be deemed small, the variation in stiffness of the descending

slope is large. This varies by a factor of four, between the largest and smallest chosen inputs.) Accordingly, s_3 was calculated to give the same stiffness for the descending slope as for the ascending slope, but with the opposite sign.

4.3. Individually calibrated parameters

The parameters τ_f , s_{y2} and s_2 were calibrated for each beam. The most significant results of the FE analyses for each are described below.

4.3.1. Residual bond stress for unyielded zone, τ_f

The residual bond stress for unyielded zones, τ_f , determined the remaining load capacity after the end-slip of the corresponding bar. As stated above, in most of the beam tests, slipping of the two tensile bars did not start simultaneously, but rather one after the other. This caused two decreasing stages in the load–deflection curve of the beam: (1) When the first bar started to slip, the load capacity decreased and the residual load capacity basically relied on the residual bond stress of that bar and maximum bond stress of the other bar and (2) after slipping of the second bar, the residual load capacity relied on the residual bond stress of both bars, see Table 3. Therefore, the first bar to slip was calibrated first.

4.3.2. Slip corresponding to residual bond stress for yielded zone, s_{y2}

The slip corresponding to residual bond stress for the yielded zone, s_{y2} , had a critical influence on the mid-span deflection at end-slip of the bar. Increasing s_{y2} from 0.25 mm to 0.45 mm delayed slipping of the bar (see Table 3); in other words, the beam deflection at end-slip increased. This is because the greater bond stresses delayed the anchorage failure.

4.3.3. Slip at the end of maximum bond stress for unyielded zones, s_2

As may be seen in Table 3, the slip at the end of maximum bond stress for unyielded zones, s_2 , governed the mid-span deflection of the beam at end-slip significantly. Large s_2 values resulted in a longer plateau in the load–deflection curve. This is reasonable, since increasing s_2 values meant that the bar would maintain high local bond values in relatively large slips.

4.4. Verification of calibrated parameters

As an example of what was compared and verified for all analysed beams, the results of the FE analyses of beam 17F (with calibrated parameters) are presented below and compared with the experimental results.

4.4.1. Load versus mid-span deflection and crack pattern

The load versus mid-span deflection from testing and FE analyses of beam 17F is shown in Fig. 13. In both test and analysis, the beam behaviour was governed by the appearance of a bending crack at mid-span followed by yielding of the tensile reinforcement bars. Thereafter, the applied load remained approximately constant, up to a mid-span deflection of 13.3 mm in testing and 13.6 mm in FE analysis (when the top inner (TI) bar at the full support (FS) side slipped). At a deflection of 19.1 mm (test) and 19.2 mm (FE analysis), the top outer (TO) bar at the narrow support (NS) also slipped. Note that the bars are named based on their original position on the bridge and that beam 17F was tested upside down. As may be seen in Fig. 13, the agreement between the analysis and the experiment is very good. The model was able to capture the overall beam response during all stages, including cracking, maximum load, remaining load and deflection when end-slip of the various bars occurred.

Fig. 14 shows the crack pattern in both the outer and inner sides of beam 17F, as recorded at the end of the test ($\Delta_m = 23.3$ mm). The crack pattern on the outer side of the beam was captured using digital image correlation (DIC), while that on the inner side was measured after testing. On the outer side, one major bending crack was located at

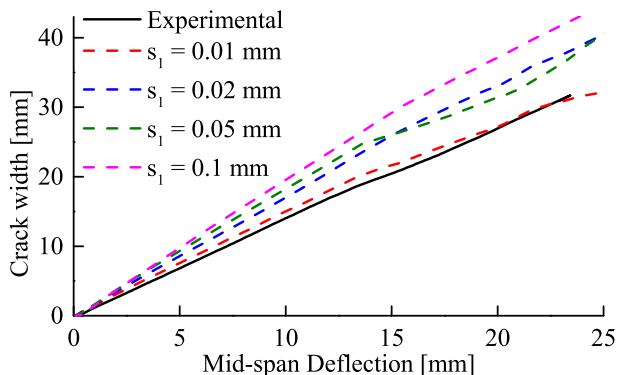


Fig. 11. The measured crack width is compared to the crack width in the analyses with different s_1 values. All results are plotted against mid-span deflection.

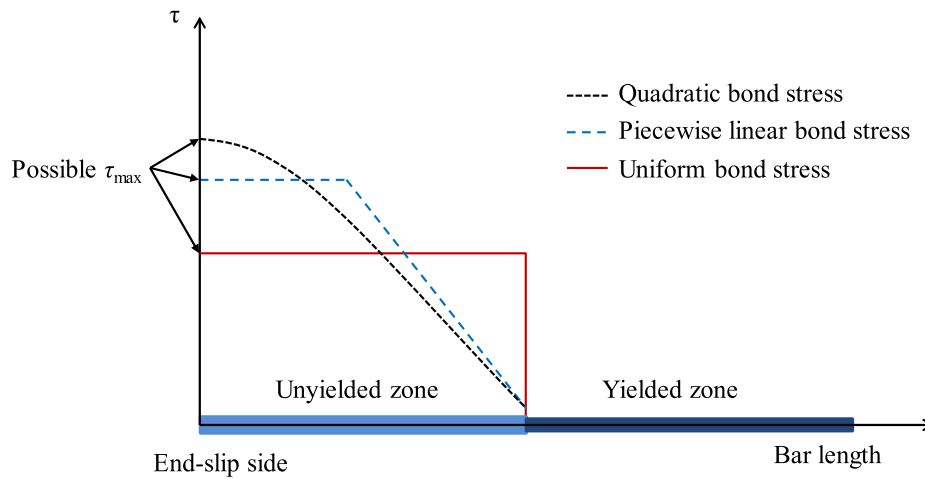


Fig. 12. Examples of different bond distributions along the unyielded zone, at the slip side before end-slip.

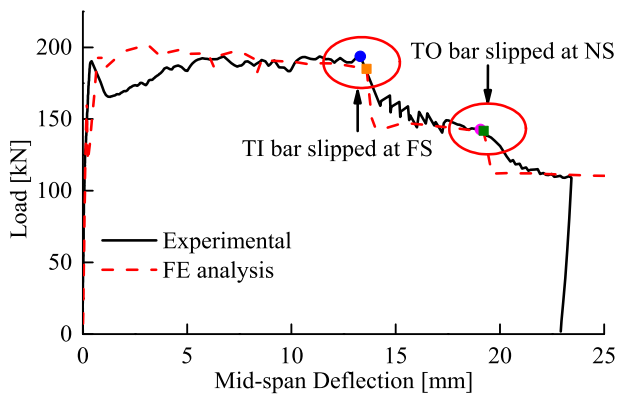


Fig. 13. Comparison of load versus mid-span deflection response for beam 17F; experimental and calibrated FE analysis results.

approximately mid-span, while a minor crack may be observed to have developed on the left side. Only one bending crack formed on the inner side. Good agreement was shown between the FE results and the observed crack pattern. The crack width was also in good agreement, as shown earlier in Figs. 8, 10 and 11. Note that the crack width compared in these figures corresponded to the crack width of the major bending crack, as measured by DIC on the outer side of the beam at reinforcement level. The values measured for the crack width were 31.5 mm (outer side) and 30.7 mm (inner side). The FE analysis results were similar to the experimental ones, at 31.2 mm (outer side) and 28.3 mm (inner side).

4.4.2. Bar stress and bond behaviour

Tensile stress, bond stress and slip along the length of the studied bar at three different loading stages (cracking, bar yielding and failure) are shown in Figs. 15 and 16. The yield penetration in the FE analyses increased from the onset of yielding until slip occurred. At this point, the yield penetration in the analyses was in good agreement with the experimental measurements of length and position.

The changes in bond behaviour along the length of the bar aligned well with the changes in its tensile stress distribution at the various loading points. At cracking, good bond conditions allowed for transfer of stresses between the reinforcement and its surrounding concrete. Thus, the stress in the bar was symmetrical, decreasing with the distance from the centre of the bar (Fig. 15) and following the bending moment distribution. The bond stress did not reach the maximum bond stress in either the yielded, $\tau_{y\max}$, or unyielded, τ_{\max} , zones. The opening of the

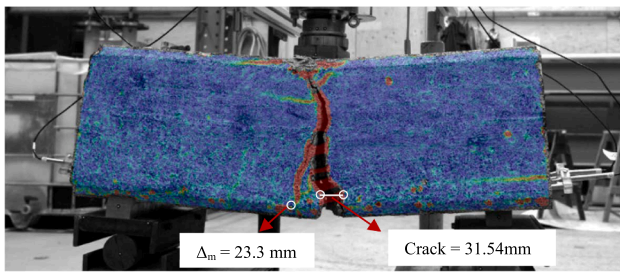
bending crack is clearly visible in Fig. 16a, as characterised by an initial bar slip at the crack location.

Under increased loading, the main crack opened, leading to increased slip at the crack location. Simultaneously, the bond stress reached the residual values, τ_{yf} and τ_f in some parts. Note that abrupt changes in bond stress distribution occurred at the transition between yielded and unyielded zones, as these regions were assigned different bond-slip relationships in the model, see Fig. 16b. These abrupt changes may not be fully realistic as, at this point of loading, the bar was not yet yielding along the entire length assigned to the yielded zone. Thus, this behaviour is a direct consequence of the modelling choice of a predefined yielded zone. Avoiding this behaviour would require a far more complex model.

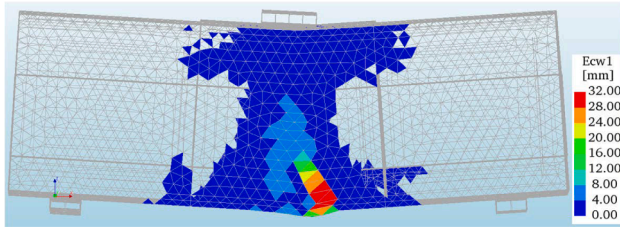
Fig. 16c shows slip and bond stress distribution in the load step just before end-slip occurred. At this load step, it may be observed that the bond along the whole yielded zone had reached the residual value, τ_{yf} and that the bar is fully yielded in the predefined region (Fig. 15). The loss of bond in the mid-region of the beam, the yielded part, indicated a transition in structural behaviour from beam to arch action. This may also be seen in Fig. 15, where the bar stress in the yielded zone was almost constant.

The transition from beam to arch action was previously observed in the experiments, [11], and has been reported by other researchers for similar cases. Feldman and Bartlett [10] recorded the variation in bar tension force and bond stress at different load levels, for a beam reinforced with plain bars. They observed near-complete bond loss in the central region of the beam, corresponding to the yield penetration. With increasing applied load, increased arch action within the mid-span brought the location of the calculated peak bond stress towards the support reactions, ultimately causing anchorage failure. Furthermore, in Coronelli and Gambarova's [20] modelling of simply supported corroded reinforced concrete beams, there was a complete bond loss in the midspan and stress redistribution at the ultimate limit state; this caused an arch action in the beam.

To conclude, the above comparisons showed that the FE analyses of 1D bond-slip relationships were capable of reasonable representation of beam behaviour. In particular, the changed load-carrying mechanism from beam to arch action and the asymmetric development of the bar yield penetration were clearly captured. This showed that the adopted bond-slip relationships were well-calibrated, thus lending confidence to the calibration procedure. However, it should be noted that the division in yielded and unyielded zones that was made during the analyses was based on the experimental results. In other words, the yield penetration was assumed a priori. Such data may not be generally (routinely) available. Nevertheless, it is clear that both the loss of bond at yielding and the asymmetry of yield penetration were very important in correctly



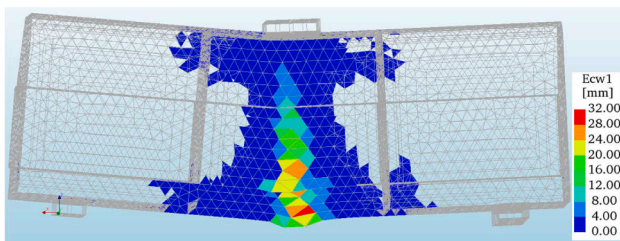
(a) Crack pattern in the outer side from DIC measurement



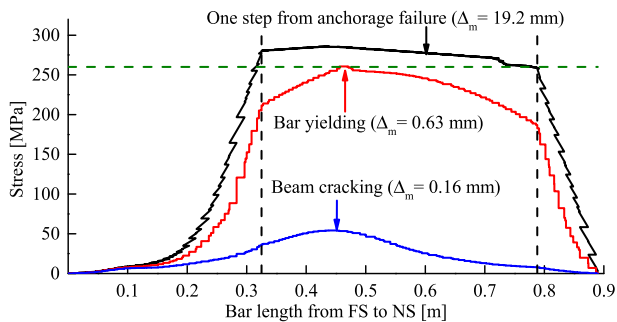
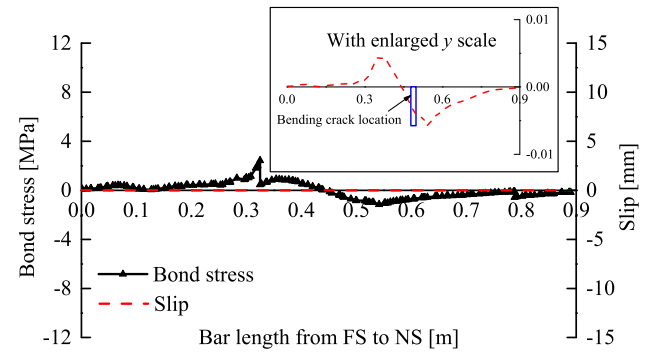
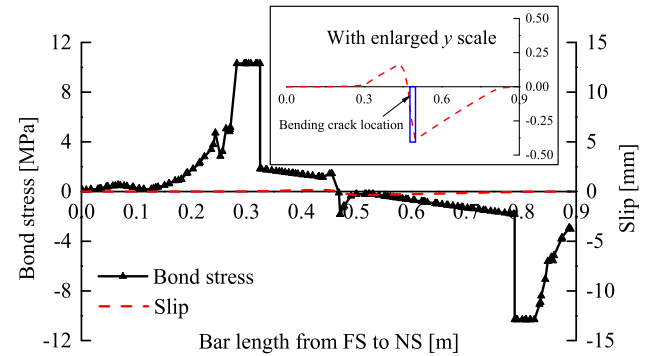
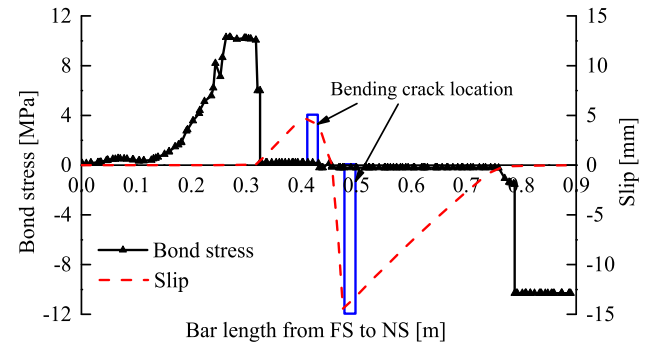
(b) FE crack pattern in the outer side



(c) Experimental crack pattern on the inner side, as measured.



(d) FE crack pattern on the inner side.

Fig. 14. Comparisons of crack patterns of beam 17F after loading ($\Delta_m = 23.3$ mm).**Fig. 15.** Variations of the stresses in the bar (TO) along the bar length. The dashed black lines mark the positions of the yield penetration in the experiment. The dashed green line represents the yield stress of the bar. (For interpretation of the references to colour in this figure legend, the reader is referred to the web version of this article.)(a) At cracking ($\Delta_m = 0.16$ mm).(b) At yielding ($\Delta_m = 0.63$ mm).(c) Just before end-slip occurred ($\Delta_m = 19.2$ mm).**Fig. 16.** Variations in bond stress and slip along TO bar in the analysis of beam 17F.

describing the structural behaviour. The asymmetrical yield penetration caused one of the sides to have a shorter available anchorage length and was thus crucial in the anchorage failure. It is common to use the symmetry of the test set-up and only model half the beam; this would not have worked when describing the asymmetric yield penetration for the studied beams. This therefore warrants further attention in future studies.

5. Results and discussion

The parameters in the bond-slip relationships were calibrated according to the procedure described in Section 4, for eighteen bars in nine beams. This section firstly presents and discusses the results of the FE analyses of the beams. The calibrated bond-slip parameters are then presented and discussed.

5.1. Overall numerical results

Exemplary comparisons between FE analyses with calibrated bond-

slip relationships and experimental results are presented in Fig. 17. Agreement is judged on the basis of load versus mid-span deflection responses and on the yielding penetration along the length of the bar at failure.

The FE analyses results for the nine beams were compared to the experimental results in Table 4 and Fig. 18. Mid-span deflection at end-slip, load capacity at end-slip and yield penetration and asymmetry were compared. Overall, the FE analyses agreed well with the test results, indicating that the final calibrated bond-slip curves were reasonable. However, some disagreement may be observed. The load capacity at end-slip of bar 16H TI was slightly too large (19%) but was too low for bar 10I TO (−20%). However, the load capacity at end-slip depended, not only on the calibrated bond-slip parameters, but also largely on the concrete compressive strength. In the analyses, the compressive strength of the concrete was assumed to be the same for all beams. Nevertheless, in reality, it varied depending on the deteriorated state and the observed high scatter in concrete properties [11]. As the other important parameters (mid-span deflection at end-slip, yield penetration and asymmetry) agreed well, the calibration of bond-slip parameters was deemed acceptable also for the bars in these beams.

5.2. Bond-slip relationships in FE analyses

Fig. 19 shows the calibrated bond-slip relationships for the unyielded zones in all bars (values in Appendix). The results for top-cast bars are plotted in the upper part and the results for bottom-cast bars are plotted in the lower part. Due to the uncertainties in the evaluation of the average corrosion level, corrosion levels lower than 0.5% were assumed to be uncorroded.

The maximum bond stress for unyielded zones (τ_{\max}) was defined as the average bond strength calculated in the experimental study [11]. Thus, similar findings to those reported there may also be observed here; top-cast bars generally had a lower τ_{\max} than bottom-cast bars when uncorroded but gained bond stress when corroded. τ_{\max} increased from 9.7 MPa to 13.4 MPa in top-cast bars, as the corrosion level increased from 0.57% to 4.7%. This may likely be attributed to the lower density of the concrete surrounding top-cast bars, which allowed for greater amounts of corrosion products to expand without spalling the surrounding concrete. Bottom-cast bars, on the other hand, lost bond stress when corroded. There was a 48.2% reduction in τ_{\max} when the corrosion level increased from 0.73% to 3.71% for bottom-cast bars. This was also confirmed in a later investigation into local bond-slip, which was also based on specimens extracted from Gullspång Bridge [16]. Moreover, the τ_{\max} values in the bars which failed in anchorage before yielding were significantly lower than those which reached yielding.

When compared with previous bond-slip constitutive models, one main difference can be observed: the maximum bond stress is considerably higher than in the constitutive models in Fig. 1, which yield a value between 1 and 2 MPa for the reinforcing bars in Gullspång bridge. This difference may be due to the models intending to provide values on

the safe side. The calibrated slip at peak agrees with the value of the model by Feldman and Bartlett [10], 0.01 mm, while this value is larger in the other models (0.1 mm in Model Code [34] and 0.23 mm in Verderame et al. [38]); it is noted that they are comparable to the slip at the end of the plateau in the calibrated curves. The calibration of the parameter s_2 was an important part of the calibration process and had large influence on the structural behaviour of the beam. This indicates that the use of fixed values for the slip in bond-slip constitutive models may not be appropriate, especially if the effect of corrosion is to be taken into account.

Further, in Fig. 19, it may be observed that a higher τ_{\max} was accompanied by a higher residual bond stress (τ_f) and a shorter plateau (s_2-s_1). This is further investigated in Fig. 20, which shows τ_f and s_2 versus τ_{\max} . As may be seen in Fig. 20a, the residual bond stress increased with the maximum bond stress, along an almost linear trend. Spalling of concrete cover decreased the residual bond stress, while splitting cracks did not have any significant effect. In Fig. 20b, it may be seen that the slip parameter s_2 decreased with the maximum bond stress. For the bars that slipped without yielding, the slip parameter s_2 was smaller than for the others. This behaviour was anticipated, as the low maximum bond stress and short plateau (small s_2) caused the early anchorage failure in bars that did not reach yielding.

Although there were four parameters in the bond-slip relationship for yielded zones, three of them were determined as constant (Section 4.1). The slip parameter s_{y2} appears in Fig. 21, plotted against parameter s_3 . Both these parameters describe the slip at the beginning of the residual bond stress. The slip parameter s_{y2} increased with s_3 . In other words, slip at residual bond stress was greater in the yielded zone when it was large in the unyielded zone. The slip parameters, s_{y2} and s_3 , were closely related to the mid-span deflection at end-slip. Ductile deformation of the beam led to a ductile behaviour in the bond-slip relationship of the bar. This trend was almost unaffected by the corrosion level, damage level or casting position. Since the test results of mid-span deflection at end-slip were highly scattered among the beams, so were the calibrated slip parameters, s_{y2} and s_3 .

5.3. Comparison of calibrated bond-slip curves with pull-out test results

It is worth to note that the described procedure to calibrate bond-slip relations from beam test results is time-consuming; and also the experiments on beams require rather large efforts. An alternative structural test method was developed and used in a previous paper by the authors [16], in the form of pull-out tests of plain bars with specimens taken from the same bridge. Details on the testing procedure can be found in the aforementioned paper. Pull-out tests are much quicker and easier both to perform and to evaluate bond-slip relations from; it is therefore of interest to compare the results from these two methods.

In Fig. 22, the average peak bond strength over a corrosion interval of 0.5% is presented, both for bottom and top-cast bars. Experimental results from pull-out tests and 3-point bending tests are compared. The

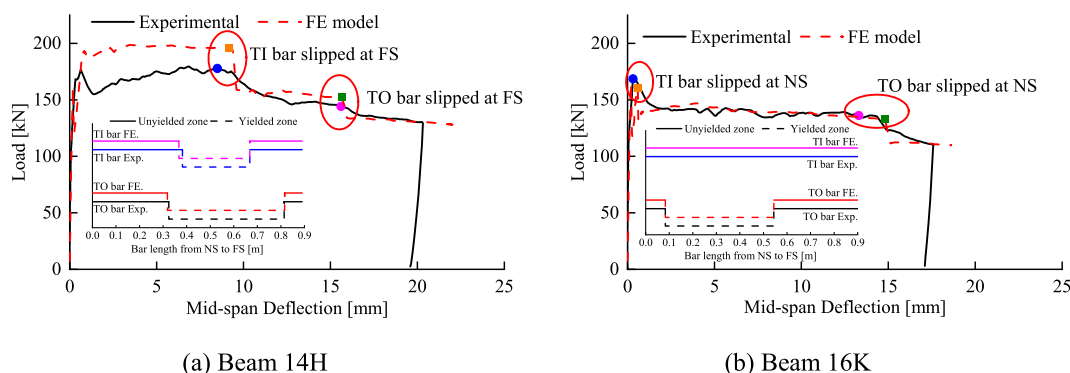
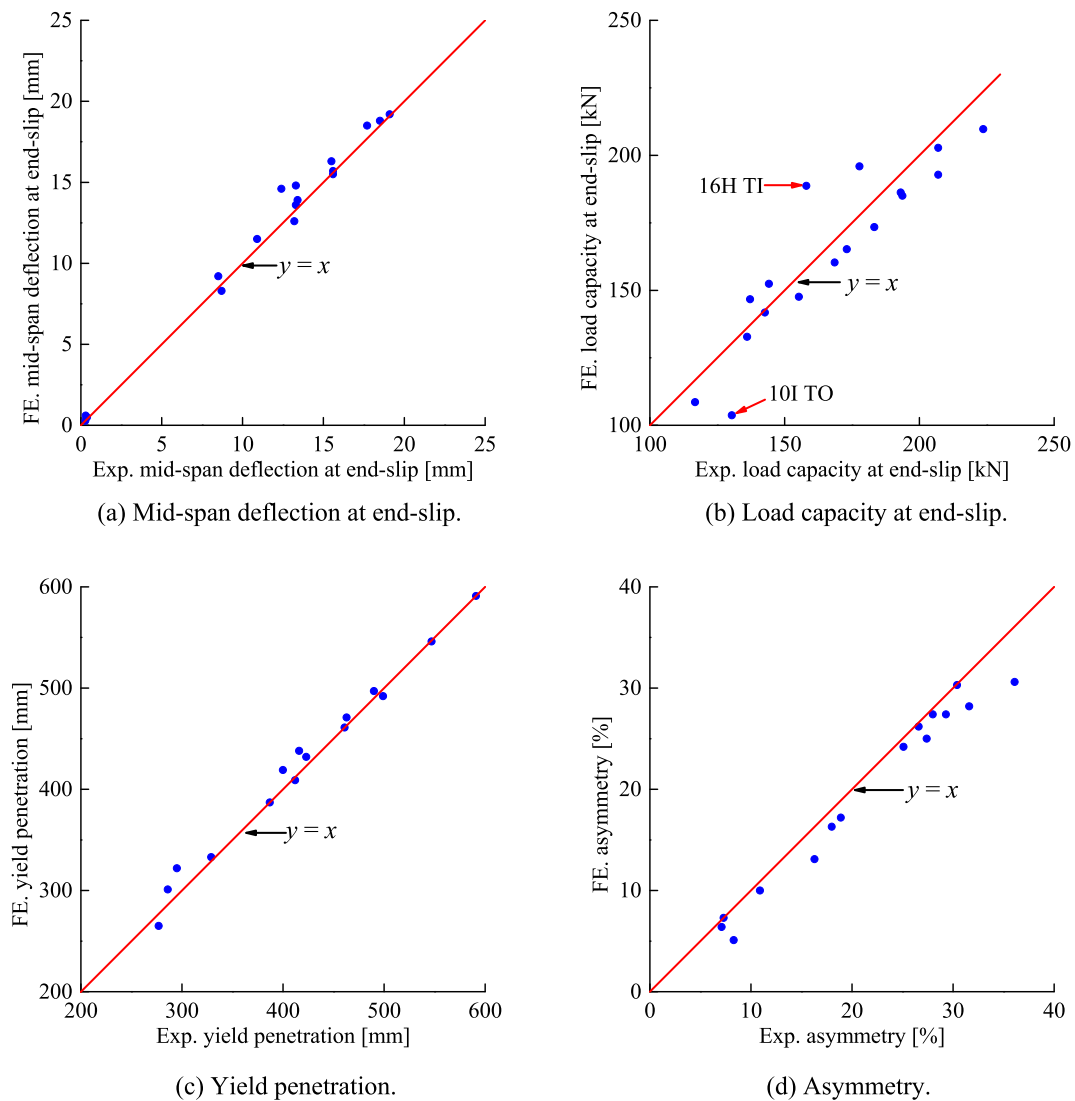


Fig. 17. Comparisons between FE analyses and experimental results for two of the analysed beams.

Table 4

Comparisons between FE analyses and experimental results in the calibration.

Beam	Bar	Mid-span deflection at end-slip (mm)			Load capacity at end-slip (kN)			Yield penetration (mm)			Asymmetry factor(%)		
		Exp.	FE.	Error (%)	Exp.	FE.	Error (%)	Exp.	FE.	Error (%)	Exp.	FE.	Error (%)
17F	TI	13.3	13.6	2.26	193.7	185.0	-4.49	423	432	2.13	29.3	27.4	-6.48
	TO	19.1	19.2	0.52	142.7	141.8	-0.63	463	471	1.73	25.1	24.2	-3.59
17H	BO	13.4	13.9	3.73	207.0	192.8	-6.86	499	492	-1.40	7.1	6.4	-9.86
	BI	17.7	18.5	4.52	155.3	147.6	-4.96	547	546	-0.18	10.9	10.0	-8.26
9D	BO	13.2	12.6	-4.55	223.7	209.7	-6.26	295	322	9.15	16.3	13.1	-19.63
	BI	13.2	12.6	-4.55	223.7	209.7	-6.26	387	387	0.00	36.1	30.7	-14.96
10I	TI	0.28	0.28	0.00	116.8	108.6	-7.02	a	\		\	\	
	TO	0.38	0.49	28.95	130.4	103.7	-20.48	\	\		\	\	
13D	TO	15.6	15.5	-0.64	193.1	186.2	-3.57	400	419	4.75	31.6	28.2	-10.76
	TI	18.5	18.8	1.62	183.3	173.4	-5.40	591	591	0.00	7.3	7.3	0.00
16B	TI	10.9	11.5	5.50	207.0	202.8	-2.03	329	333	1.22	26.6	26.2	-1.50
	TO	15.5	16.3	5.16	173.1	165.2	-4.56	416	438	5.29	27.4	25	-8.76
16H	TI	8.7	8.3	-4.60	158.1	188.7	19.35	277	265	-4.33	8.3	5.1	-38.55
	TO	12.4	14.6	17.74	137.2	146.7	6.92	412	409	-0.73	18.9	17.2	-8.99
16K	TI	0.3	0.6	100.00	168.6	160.3	-4.92	\	\		\	\	
	TO	13.3	14.8	11.28	136.1	132.8	-2.42	461	461	0.00	30.4	30.3	-0.33
14H	TI	8.5	9.2	8.24	177.8	195.9	10.18	286	301	5.24	18.0	16.3	-9.44
	TO	15.6	15.7	0.64	144.2	152.4	5.69	490	497	1.43	28.0	27.4	-2.14

^a Bar slipped without yielding.**Fig. 18.** Comparisons of FE analyses, with calibrated bond-slip as input, and experimental results.

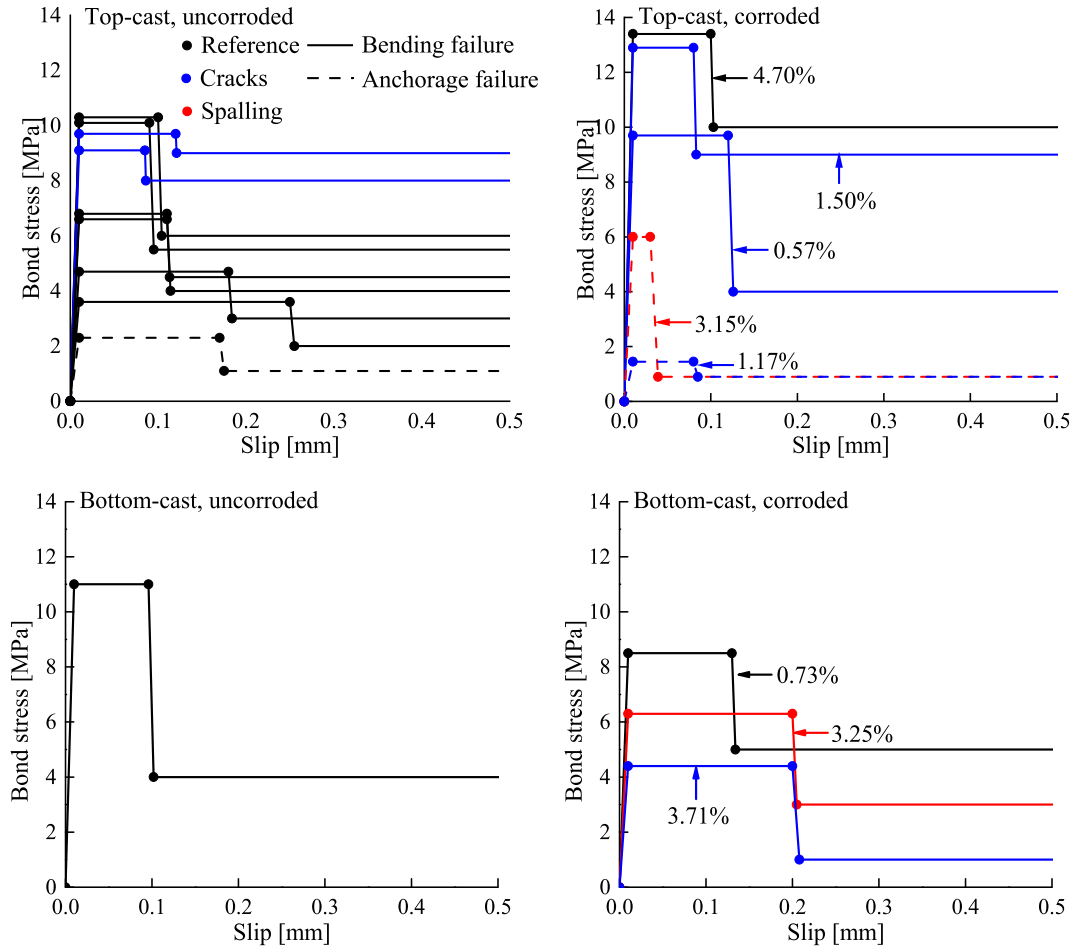


Fig. 19. Calibrated bond stress versus slip for unyielded zones in bars. All results are divided by casting positions and the presence of corrosion. The average corrosion level of 0.5% is used to distinguish between corroded and uncorroded bars. The damage level of each anchorage zone is displayed by colours. Bars with no yielded zone (which slipped before they reached yielding) are marked with a dashed line.

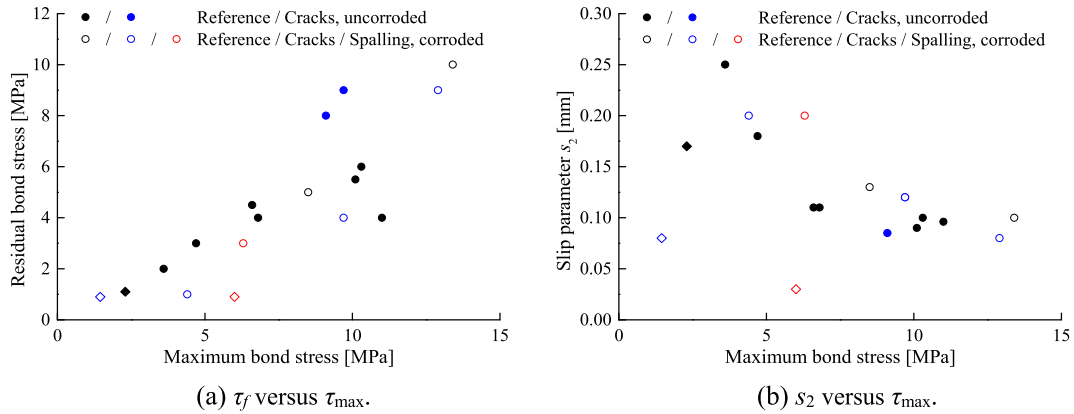


Fig. 20. (a) Residual bond stress versus the maximum bond stress and (b) slip at the end of maximum bond stress plateau for unyielded zones versus maximum bond stress. The damage level in each anchorage zone is shown using colours. The uncorroded bars are marked with filled dots, and the corroded ones are marked with unfilled dots. Bars that failed in anchorage before yielding are marked with lozenges.

tests results are shown to follow a similar trend, both for top- and bottom-cast bars. The average peak bond strength recorded in the pull-out tests is consistently lower than in the 3-point bending tests. Such observation indicates that the acquired data are likely to be on the safe side. Thus, the authors believe that pull-out tests could be a useful, fast and cheap option for acquiring data on existing structures. Average bond strength is shown to well correspond to structural tests results both in

trends and order of magnitude in Fig. 22.

In Fig. 23, the residual bond strength, as obtained from the calibration of the bond-slip curves in this work, is plotted against the maximum bond strength, re-presenting data from Fig. 20a. Additionally, the residual bond strength as obtained from the pull-out tests (defined as the bond stress recorded at 4.5 mm of slip) is presented against the recorded maximum bond strength. Only results from top-cast bars were chosen,

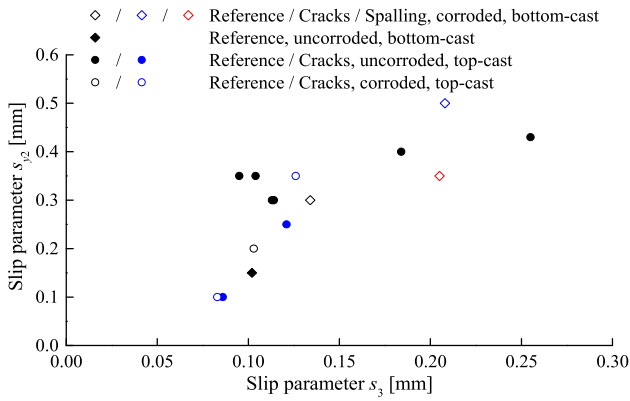


Fig. 21. The slip parameter s_{y2} against slip parameter s_3 . The damage level in each anchorage zone is shown by colours. The uncorroded bars are marked with filled dots, and the corroded ones are marked with unfilled dots. Different shapes indicate the casting position of the bars.

given the more significant amount of data obtained in the FE analyses. Two linear interpolations are presented for reference bars, one for pull-out data and one from FE results. The choice of reference bars is again based on the amount of data points.

Pull-out tests and calibrated FE analysis results of the beams show good agreement, both in magnitude and in trend. This is particularly of interest, since residual bond strength is hard to define experimentally from 3-point bending tests, but easy to obtain with pull-out tests. Nevertheless, the use of FE analyses allowed us to define the residual bond strength in the beam tests, and, thus, to compare it with the pull-out tests results. Fig. 23 confirms what already observed in Fig. 22, indicating pull-out tests results as a reasonable choice for characterising the bond of plain bars. The data acquired present, however, a significant scatter, and individual pull-out test results are not always on the safe side with respect to behaviour in beams. This needs to be taken into account if it is chosen to employ data acquired from pull-out tests to define the residual bond of plain bars. Additionally, it is important that such comparison takes place between specimens with similar characteristics, such as the absence of corrosion induced cracks in the concrete cover, as in this case, or similar estimated corrosion levels. The acquisition of additional data, on different existing structures, is however

necessary for reaching a better understanding on the usability of pull-out tests for structural assessment.

6. Conclusions

This work aimed to gain insights into the effect of corrosion and yielding of plain reinforcement bars on the bond and structural behaviour of RC beams. A total of nine previously tested beams were analysed using 3D NLFEA. Each tensile reinforcement bar was divided into yielded and unyielded zones, with different 1D bond-slip relationships assigned. The bond-slip parameters which characterised these curves were carefully calibrated. From the results and the calibration of the bond curves, the following conclusions may be drawn:

1. The FE analyses with calibrated 1D bond-slip relationships might provide a consistent description of the behaviour of the damaged RC beams with plain bars. Load-deflection curve, crack pattern, load-carrying mechanism and asymmetrical yielding development agreed well with the experimental results. Thus, the shape used for the bond-slip relationship was suitable and the chosen parameters were adequately calibrated to describe the interaction between concrete and corroded plain bars.
2. Nine bond-slip parameters were needed for each bar (Fig. 7). Four parameters (τ_{max} , τ_{yf} , s_{y1} and s_1) might be set as constant for all bars, while two other parameters (τ_{max} and s_3) might be manually calculated from test results and the other parameters. Only three parameters, τ_f , s_{y2} and s_2 , needed to be individually calibrated for each bar, by comparing FEA and experimental results. Further, τ_f and s_2 were correlated to τ_{max} , which simplified the calibration process.
3. For the bond-slip relationships for unyielded zones, a higher maximum bond stress was followed by a shorter plateau and higher residual bond stress. Spalling of concrete cover decreased the residual bond stress, while splitting cracks did not have any significant effect.
4. A main finding of this study was that, to be able to describe the structural behaviour adequately, the loss of bond at yielding and the asymmetry of the yield penetration were both crucial factors. Whilst the former was already reported by other researchers, the latter, to the authors' knowledge, had not been previously observed. The asymmetry of the yield penetration caused one of the sides to have a

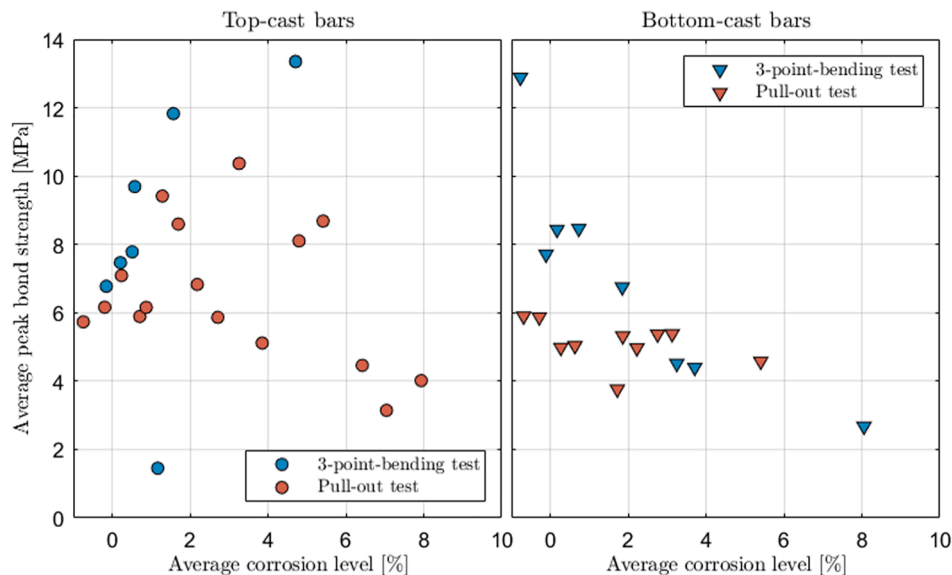


Fig. 22. Average peak bond strength and corresponding average corrosion level of top- and bottom-cast bars tested both in 3-point bending and with pull-out tests. Each point in the graph represents the bond strength of the tested bars averaged over an interval of 0.5% of corrosion.

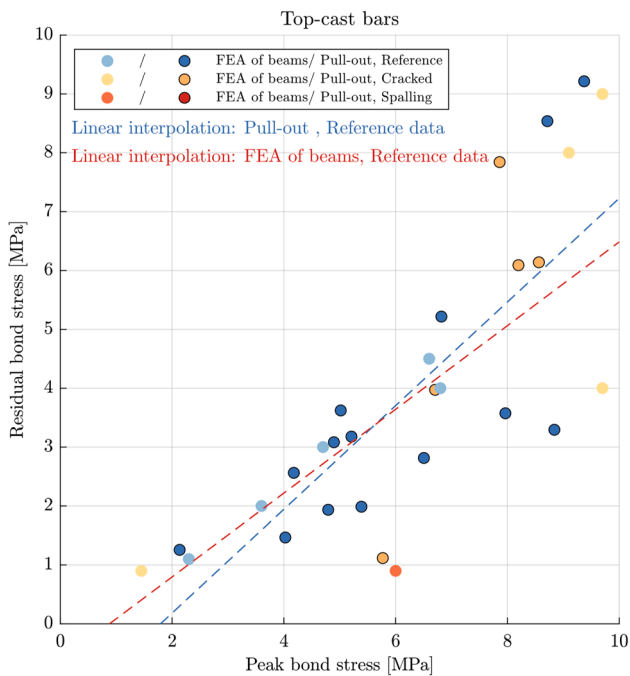


Fig. 23. Residual bond stress versus the maximum bond stress of top-cast bars, as obtained from the calibration of FE analyses of beams and pull-out test results. Results from reference specimens are linearly interpolated, for FE analysis (in orange), and for pull-out tests results (in blue). Different colours of the markers indicate different levels of damage in the surrounding concrete. (For interpretation of the references to colour in this figure legend, the reader is referred to the web version of this article.)

shorter available anchorage length. This, therefore, governed the anchorage failure mode.

To conclude, this study presents a novel approach to the assessment

of concrete structures with plain bars. The use of FE models to interpret structural tests on naturally corroded structures showed the importance of including the bond behaviour of plain bars for a correct assessment, and specifically, highlighted the effect of loss of bond at yielding and the asymmetric behaviour of the yield penetration. This is particularly of interest since it is common to utilize symmetries in a structure to reduce computational cost. This could lead to a significant overestimation of the anchorage length. In the presented analyses, the position of the yield penetration was assumed as an input parameter based on measurements from experiments. This is an important limitation, as it is an unknown parameter a priori. However, observations on the asymmetry in the distribution of the yield penetration are given and could be used to estimate a possible reduction of the unyielded length. Additionally, comparisons with pull-out test results suggest that they can provide useful information to calibrate the bond-slip curve of plain bars; however, this deserves more attention in future studies.

Declaration of Competing Interest

The authors declare that they have no known competing financial interests or personal relationships that could have appeared to influence the work reported in this paper.

Acknowledgments

The authors would like to thank Jakob Sumearll, visiting researcher at Chalmers during the same period as the first author, for his suggestions and support on the FE analyses. Also, the first author has been supported by the Chinese Scholarship Council and the Fundamental Research Funds for the Central Universities (2018B41414). Parts of the work were also funded by the Swedish Research Council Formas and the Swedish Transport Administration. The computations were enabled by resources provided by the Swedish National Infrastructure for Computing (SNIC) at Chalmers Centre for Computational Science and Engineering (C3SE) partially funded by the Swedish Research Council through grant agreement no. 2018-05973.

Appendix

Values of calibrated bond-slip relationships for unyielded and yielded zones in all bars.

Beam	Bar	Unyielded zones					Yielded zone			
		s_1 (mm)	τ_{\max} (MPa)	s_2 (mm)	s_3 (mm)	τ_f (MPa)	s_{y1} (mm)	$\tau_{y\max}$ (MPa)	s_{y2} (mm)	τ_{yf} (MPa)
17F	TI	0.01	10.1	0.09	0.095	5.5	0.01	2	0.35	0.2
	TO	0.01	10.3	0.1	0.104	6	0.01	2	0.35	0.2
17H	BO	0.01	6.3	0.2	0.205	3	0.01	2	0.35	0.2
	BI	0.01	8.5	0.13	0.134	5	0.01	2	0.3	0.2
9D	BO	0.01	4.4	0.2	0.208	1	0.01	2	0.5	0.2
	BI	0.01	11	0.096	0.102	4	0.01	2	0.15	0.2
10I	TI	0.01	1.45	0.08	0.085	0.9	\ ^a			
	TO	0.01	6	0.03	0.039	0.9	\			
13D	TO	0.01	9.7	0.12	0.121	9	0.01	2	0.25	0.2
	TI	0.01	9.1	0.085	0.086	8	0.01	2	0.1	0.2
16B	TI	0.01	6.8	0.11	0.114	4	0.01	2	0.3	0.2
	TO	0.01	9.7	0.12	0.126	4	0.01	2	0.35	0.2
16H	TI	0.01	3.6	0.25	0.255	2	0.01	2	0.43	0.2
	TO	0.01	6.6	0.11	0.113	4.5	0.01	2	0.3	0.2
16K	TI	0.01	2.3	0.17	0.175	1.1	\			
	TO	0.01	12.9	0.08	0.083	9	0.01	2	0.1	0.2
14H	TI	0.01	4.7	0.18	0.184	3	0.01	2	0.4	0.2
	TO	0.01	13.4	0.1	0.103	10	0.01	2	0.2	0.2

^a Bar without yielded zone.

References

- [1] Lundgren K. Effect of corrosion on the bond between steel and concrete: An overview. *Mag Concr Res* 2007;59:447–61. <https://doi.org/10.1680/mac.2007.59.6.447>.
- [2] Hou B, Li X, Ma X, Du C, Zhang D, Zheng M, et al. The cost of corrosion in China. *Npj Mater Degrad* 2017;1. <https://doi.org/10.1038/s41529-017-0005-2>.
- [3] Mangat PS, Elgarf MS. Flexural strength of concrete beams with corroding reinforcement. *ACI J* 1999;96(1):149–58.
- [4] Fernandez I, Herrador MF, Marí AR, Bairán JM. Ultimate capacity of corroded statically indeterminate reinforced concrete members. *Int J Concr Struct Mater* 2018;12. <https://doi.org/10.1186/s40069-018-0297-9>.
- [5] Rodríguez J, Ortega LM, Casal J. Load carrying capacity of concrete structures with corroded reinforcement. *Constr Build Mater* 1997;11:239–48.
- [6] Yu L, François R, Dang VH, L'Hostis V, Gagné R. Structural performance of RC beams damaged by natural corrosion under sustained loading in a chloride environment. *Eng Struct* 2015;96:30–40. <https://doi.org/10.1016/j.engstruct.2015.04.001>.
- [7] Fernandez I, Berrocal CG. Mechanical properties of 30 year-old naturally corroded steel reinforcing bars. *Int J Concr Struct Mater* 2019;13. <https://doi.org/10.1186/s40069-018-0308-x>.
- [8] Feldman LR, Cairns J. Assessing historical provisions for bond of plain bars. *ACI Mater J* 2017;114:463–73. <https://doi.org/10.14359/51689163>.
- [9] Cairns J, Du Y, Law D. Structural performance of corrosion-damaged concrete beams. *Mag Concr Res* 2008;60:359–70. <https://doi.org/10.1680/mac.2007.00102>.
- [10] Feldman LR, Bartlett FM. Bond in flexural members with plain steel reinforcement. *ACI Struct J* 2008;105:552–60. <https://doi.org/10.14359/19938>.
- [11] Robuschi S, Lundgren K, Fernandez I, Flansbjer M. Anchorage of naturally corroded, plain reinforcement bars in flexural members. *Mater Struct* 2020;53. <https://doi.org/10.1617/s11527-020-01471-2>.
- [12] Feldman LR, Bartlett FM. Bond strength variability in pullout specimens with plain reinforcement. *ACI Struct J* 2005;102:860–7.
- [13] Cairns J, Du Y, Law D. Residual bond strength of corroded plain round bars. *Mag Concr Res* 2006;58:221–31. <https://doi.org/10.1680/mac.2006.58.4.221>.
- [14] Fang C, Lundgren K, Chen L, Zhu C. Corrosion influence on bond in reinforced concrete 2004;34:2159–67. <https://doi.org/10.1016/j.cemconres.2004.04.006>.
- [15] Van SC, Verstrynghe E, Wevers M, Vandewalle L. Cement and Concrete Research Assessing the bond behaviour of corroded smooth and ribbed rebars with acoustic emission monitoring. *Cem Concr Res* 2019;120:176–86. <https://doi.org/10.1016/j.cemconres.2019.03.023>.
- [16] Robuschi S, Sumearl J, Fernandez I, Lundgren K. Bond of naturally corroded, plain reinforcing bars in concrete. *Struct Infrastruct Eng* 2020. <https://doi.org/10.1080/15732479.2020.1768273>.
- [17] Austin SA, Lyons R, Ing MJ. Electrochemical behavior of steel-reinforced concrete during accelerated corrosion testing. *Corrosion* 2004;60(2):203–12.
- [18] Choi YS, Yi ST, Kim MY, Jung WY, Yang EI. Effect of corrosion method of the reinforcing bar on bond characteristics in reinforced concrete specimens. *Constr Build Mater* 2014;54:180–9. <https://doi.org/10.1016/j.conbuildmat.2013.12.065>.
- [19] Fu C, Jin N, Ye H, Jin X, Dai W. Corrosion characteristics of a 4-year naturally corroded reinforced concrete beam with load-induced transverse cracks. *Corros Sci* 2017;117:11–23. <https://doi.org/10.1016/j.corsci.2017.01.002>.
- [20] Coronelli D, Gambarova P. Structural assessment of corroded reinforced concrete beams: modeling guidelines. *J Struct Eng* 2004;130:1214–24. [https://doi.org/10.1061/\(asce\)0733-9445\(2004\)130:8\(1214\)](https://doi.org/10.1061/(asce)0733-9445(2004)130:8(1214)).
- [21] Tahershamsi M, Fernandez I, Zandi K, Lundgren K. Four levels to assess anchorage capacity of corroded reinforcement in concrete. *Eng Struct* 2017;147:434–47. <https://doi.org/10.1016/j.engstruct.2017.06.024>.
- [22] Lundgren K, Gylltoft K. Model for the bond between concrete and reinforcement. *Mag Concr Res* 2000;52:53–63. <https://doi.org/10.1680/mac.2000.52.1.53>.
- [23] Lundgren K. Bond between ribbed bars and concrete. Part 2: The effect of corrosion. *Mag Concr Res* 2005;57:383–95. <https://doi.org/10.1680/mac.2005.57.7.383>.
- [24] Lundgren K, Robuschi S, Zandi K. Methodology for testing rebar-concrete bond in specimens from decommissioned structures. *Int J Concr Struct Mater* 2019;13. <https://doi.org/10.1186/s40069-019-0350-3>.
- [25] Fernandez I, Lundgren K, Zandi K. Evaluation of corrosion level of naturally corroded bars using different cleaning methods, computed tomography, and 3D optical scanning. *Mater Struct* 2018;51:1–13. <https://doi.org/10.1617/s11527-018-1206-z>.
- [26] EN 12390-3:2009. Testing hardened concrete. Part 6: Tensile splitting strength of test specimens; 2009.
- [27] CEB-FIP. Fib model code for concrete structures 1990. Lausanne, Switzerland; 1993.
- [28] Diana. DIANA Finite Element Analysis, User's Manual, release 10.2. Delft, Netherlands; 2017.
- [29] Hordijk DA. Local approach to fatigue of concrete. Delft: Delft University of Technology; 1991.
- [30] Vecchio FJ, Collins MP. The modified compression field theory for reinforced concrete elements subjected to shear. *ACI J* 1986;83(22):219–31.
- [31] Selby RG, Vecchio FJ. A constitutive model for analysis of reinforced concrete solids. *Can J Civ Eng* 1997;24(3):460–70.
- [32] Engström B. Ductility of tie connections in precast structures. Gotherburg: Chalmers University of Technology; 1992.
- [33] Shima H, Chou L, Okamura H. Bond characteristics in post-yield range of deformed Bars. *Concr Libr JSCE* 1987;10(10):113–24.
- [34] CEB-FIP, fib model code for concrete structures 2010. Lausanne, Switzerland; 2013.
- [35] Mylrea TD. Bond and anchorage. *ACI J* 1948;44(3):521–52.
- [36] Chen E, Berrocal Gil Carlos, Fernandez Ignasi, Löfgren Ingemar, Lundgren Karin. Assessment of the mechanical behaviour of reinforcement bars with localised pitting corrosion by Digital Image Correlation. *Eng Struct* 2020;219. <https://doi.org/10.1016/j.engstruct.2020.110936>.
- [37] Fernandez Ignasi, Berrocal Gil Carlos. Mechanical properties of 30 year-old naturally corroded steel reinforcing bars. *Int J Concrete Struct Mater* 2019;13. <https://doi.org/10.1186/s40069-018-0308-x>.
- [38] Verderame GM, De Carlo G, Ricci P, Fabbrocino G. Cyclic bond behaviour of plain bars. Part II: Analytical investigation. *Constr Build Mater* 2009;23(12):3512–22. <https://doi.org/10.1016/j.conbuildmat.2009.07.001>.
- [39] Robuschi Samanta, Tengattini Alessandro, Dijkstra Jelke, Fernandez Ignasi, Lundgren Karin. A closer look at corrosion of steel reinforcement bars in concrete using 3D neutron and X-ray computed tomography. *Cement and Concrete Research* 2021;144. <https://doi.org/10.1016/j.cemconres.2021.106439>.